INORGANIC CHEMISTRY FRONTIERS

RESEARCH ARTICLE

View Article Online
View Journal | View Issue

Open Access Article. Published on 02 bezna 2023. Downloaded on 20.10.2024 2:06:59.
This article is licensed under a Creative Commons Attribution-NonCommercial 3.0 Unported Licence.

Check for updates

Cite this: *Inorg. Chem. Front.*, 2023, **10**, 2165

Facile, fast and green synthesis of a highly porous calcium-syringate bioMOF with intriguing triple bioactivity†

Albert Rosado,*[a] Oriol Vallcorba,[b] Blanca Vázquez-Lasa,‡[c,d] Luís García-Fernández,[c,d] Rosa Ana Ramírez-Jiménez,[c,d] María Rosa Aguilar,[c,d] Ana M. López-Periago,[a] Concepción Domingo*[a] and José A. Ayllón*[e]

Received 10th December 2022,
Accepted 1st March 2023

DOI: 10.1039/d2qi02639b

rsc.li/frontiers-inorganic

A facile, fast and green strategy based on ethanol is utilized to prepare a new bioMOF, namely, CaSyr-1, with particular characteristics of full biocompatibility given by using just calcium and syringic acid, the latter being a phenolic natural product found in fruits and vegetables, permanent porosity with an outstanding surface area >1000 m^2 g^{-1}, and a micropore diameter of 1.4 nm close to mesopore values. Collectively, these data establish CaSyr-1 as one of the most porous bioMOFs reported to date, with high molecular adsorption capacity. The CaSyr-1 adsorptive behavior is revised here through the reversible adsorption of CO_2 and the encapsulation of bioactive ingredients in the structure. Remarkably, CaSyr-1 enables the development of triple therapeutic entities, involving bioactive Ca^{2+}, syringic acid and an impregnated drug.

1. Introduction

Metal organic frameworks (MOFs) are fascinating crystalline materials with remarkably high porosity and versatile chemistry.[1] Biological MOFs, known as bioMOFs, are composed of biocompatible metals and organic biomolecules as linkers, and are suitable for applications as diverse as gas adsorption[2] and medicine.[3] The research on bioMOFs for biomedical applications, with particular interest in the development of drug delivery systems, is currently a hot topic in biomaterials science.[4] For this purpose, bioMOFs can be used either as-synthesized or after encapsulation of specific active pharmaceutical products.[5] Some interesting bioMOFs, constituted by non-toxic endogenous cations, *e.g.* Ca^{2+}, Zn^{2+}, Mg^{2+} or $Fe^{2+/3+}$, and naturally occurring ligands have already been reported.[6] Nevertheless, the integration of exclusively biocompatible units in the framework of a MOF is not a straightforward task, since most biomolecules possess low symmetry that prevents the formation of porous and stable networks, often requiring the use of (toxic) auxiliary ligands.[7] Hence, the utilization of bioMOFs in the biomedical area has been limited by the difficulties found in preparing fully biocompatible compounds, considering not only the nature of the building units, but also the size of the particles as indicators of overall cytotoxicity.[8] Regarding the latter, bioMOFs must be developed as nanoparticles, with a well-defined shape and narrow particle-size distribution, which are modulated by optimizing the experimental conditions during synthesis.[9]

An important point to consider in the development of bioMOFs is the chosen synthetic route. A typical reaction path designed to develop MOFs relies on the use of high boiling point basic solvents, as those derived from formamide, under solvothermal conditions.[10] This method is widely used because it provides crystals of high quality suitable for structural elucidation. However, the overall process generally involves harsh reaction conditions, long reaction/activation periods and large amounts of hazardous solvents that tend to get trapped in the internal cavities of the MOF, parameters that hinder not only their biomedical application, but also their scale-up production.[11] Currently, more sustainable methods are under research, such as those based on the use of non-toxic solvents, *e.g.*, water or ethanol, and applying easy scalable mechanochemical or spray-drying technologies.[12]

[a]*Institut de Ciència de Materials de Barcelona (ICMAB), Consejo Superior de Investigaciones Científicas (CSIC), Campus UAB s/n, 08193 Bellaterra, Spain. E-mail: arosado@icmab.es, conchi@icmab.es*
[b]*ALBA Synchrotron Light Source, 08290 Cerdanyoladel Vallés, Spain*
[c]*Instituto de Ciencia y Tecnología de Polímeros (ICTP), Consejo Superior de Investigaciones Científicas (CSIC), C/Juan de la Cierva, 3, 28006 Madrid, Spain*
[d]*Networking Biomedical Research Centre in Bioengineering, Biomaterials and Nanomedicine (CIBER-BNN), Av. Mon-forte de Lemos, 3-5, 28029 Madrid, Spain*
[e]*Departament de Química, Universitat Autònoma de Barcelona (UAB), Campus UAB s/n, 08193 Bellaterra, Spain. E-mail: JoseAntonio.Ayllon@uab.es*

† Electronic supplementary information (ESI) available: Crystal structure description, additional figures (S1–S12) and tables (S1–S4). CCDC 2214086. For ESI and crystallographic data in CIF or other electronic format see DOI: **https://doi.org/10.1039/d2qi02639b**

‡ This author is deceased.

Open Access Article. Published on 02 bezna 2023. Downloaded on 20.10.2024 2:06:59.
This article is licensed under a Creative Commons Attribution-NonCommercial 3.0 Unported Licence.

To advance the molecular design and synthetic aspects of bioMOFs, this work presents a facile, fast and green strategy for the preparation of a novel porous 3D framework, named here as CaSyr-1, composed of a calcium cation (Ca^{2+}) as the metal node and a syringate dianion (Syr^{2-}) as the organic linker (Fig. 1), with unique textural properties and intriguing sorption and biomedical applications.

The incorporation of Ca^{2+} into MOFs has recently gained significant attention, with more than 150 crystal structures already reported.[13] This interest is attributed to multiple health benefits,[14] together with the mostly unexplored unique properties that this cation can provide, which are different from the well-known features of the universally employed transition metals. Syringic acid (H_2Syr) is a phenolic compound, often found in fruits and vegetables, with anti-oxidant, anti-inflammatory, anti-cancer and anti-hypertensive therapeutic properties.[15] Contrary to Ca^{2+}, the utilization of Syr^{2-} in coordination chemistry has been scarce and absent in porous compounds.[16]

2. Results and discussion

2.1. Synthesis

Porous CaSyr-1 nanopowder was synthesized in this work with a large space–time yield following an eco-friendly route in the green solvent ethanol (EtOH).[17] Remarkably, the material could be prepared in only a few min (*i.e.*, 10 min) by simply mixing quantitative molar amounts of reactants, calcium acetylacetonate ($Ca(acac)_2$) and H_2Syr, in a reduced volume of the solvent (1 mmol of each reactant in 1 or 10 mL of EtOH, corresponding to reactants : EtOH with molar ratios of 1 : 8 and 1 : 80, respectively) at room temperature. Powder X-ray diffraction (PXRD) indicates that the obtained product was in both cases the explored phase CaSyr-1 (Fig. 2a and S1† for 1 : 80 and 1 : 8 molar ratios, respectively). However, narrow particle-size distributions, most appropriate for biomedical uses, were obtained in the system with an increase in the volume of EtOH (Fig. 2b, c and S2, S3†), which allows a better control over supersaturation and subsequent nucleation and crystal growth. CaSyr-1 was thus precipitated as isometric porous nanoparticles with a mean diameter of 64 ± 11 nm (Fig. 2b and c). According to dynamic light scattering (DLS) measurements, the mean hydrodynamic diameter in suspension was *ca.* 150 nm when suspended in EtOH (Fig. S4†). Moreover, the particle-size distribution was extremely narrow (100–200 nm), which indicates that CaSyr-1 exhibits adequate dimensional properties for biosystems designed for flowing in blood vessels.[18] The synthetic protocol was optimized to reduce the cost and time of the process, but conserving the desired dimensional, morphological and textural properties of the end product.

Fig. 1 Occurrence and bioactivity of CaSyr-1 building blocks.

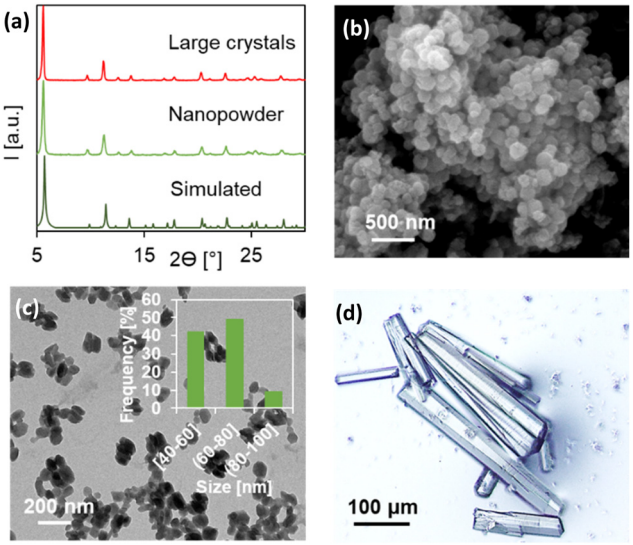

Fig. 2 (a) PXRD pattern of CaSyr-1 species compared with the simulated, (b) SEM and (c) TEM with the particle size histogram of the nanopowder, and (d) an optical microscope image of large crystals.

2.2. Crystal structure

In order to elucidate the crystalline structure of CaSyr-1, crystals of suitable quality (Fig. 2d) were prepared in dimethylformamide (DMF) at 393 K and characterized by synchrotron XRD. The resolved crystalline structure has the formula $[Ca_2(Syr)_2(H_2O)_2]_n\subset$(solvent), which was confirmed by elemental analysis (Table S1†). A simulated PXRD pattern from the single crystal data matched those of both bulk large crystals precipitated in DMF and the nanopowder obtained in EtOH (Fig. 2a). The CaSyr-1 framework consists of interconnected dimeric units containing two crystallographically independent Ca^{2+} ions, two independent Syr^{2-} linkers and two ancillary H_2O ligands (Fig. 3a). A detailed description of the crystalline structure can be found in the ESI.† Briefly, regarding the calcium sphere, it is worth highlighting the double clamp-like coordination mode of Syr^{2-} that is responsible for the connection between Ca1 and Ca2 (through two μ_2-oxo bridges, O2 and O5) and, thus, for the formation of the dimer. This coordination mode is powered by the adjacent methoxy-phenolate-methoxy groups present in the ligand. Although isolated methoxy groups are extremely weak ligands, when positioned next to a coordinating group, such as phenolate, they tend to form this robust clamp-like coordination.[19] With respect to syringate, the role of the dicarboxylate groups is also noteworthy in the extension of the structure (Fig. 3b), since they serve as

Open Access Article. Published on 02 bezna 2023. Downloaded on 20.10.2024 2:06:59.
This article is licensed under a Creative Commons Attribution-NonCommercial 3.0 Unported Licence.

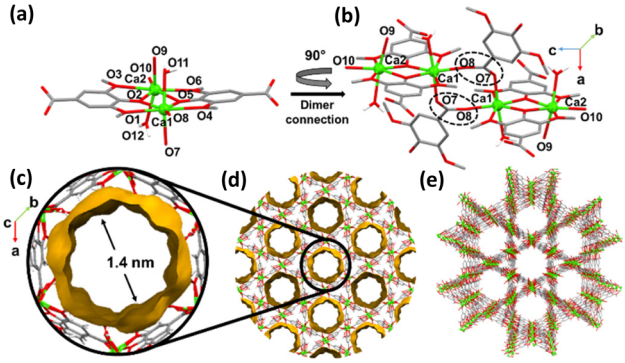

Fig. 3 Structure of CaSyr-1: (a) dimeric unit, (b) connections through dicarboxylate bridges, (c) pore structure, (d) void arrangement, and (e) 3D framework.

bridges of two different dimeric units and promote the formation of the 3D porous framework (Fig. 3c–e). The resulting network displays two types of prisms, triangular and hexagonal (ratio 2 : 1), with a disposition in the space that resembles the Kagome lattice, frequently found in natural minerals, but also in many MOFs.[20]

Void volume measurement using Mercury software (probe radius 1.2 Å) indicates that the porosity arises only from the hexagonal section, in the form of unidimensional channels with a diameter of 1.4 nm. Note that CaSyr-1 has the largest pore diameter value described for microporous bioMOFs, close to that of mesoporous bioMOFs.[21] Additionally, a highly porous architecture of open pores is obtained, with 36 v% void space.

2.3. Porosity and thermal stability

CaSyr-1 porosity was experimentally confirmed by N_2 physisorption at 77 K, giving an isotherm of type I (Fig. 4a). The high adsorption values at a very low relative pressures indicate microporosity (micropore volume of 0.32 $cm^3\ g^{-1}$), which is in accordance with the size of the cavities observed in the resolved crystalline structure. N_2 uptake at high relative pressures, accompanied by hysteresis, is assigned to interparticle mesoporous voids. A high value of an apparent BET surface area of 1080 $m^2\ g^{-1}$ (Langmuir 1205 $m^2\ g^{-1}$) was derived from the isotherm, which is exceptional in comparison with other reported bioMOFs that are considered totally biocompatible (Table 1), as CaSyr-1, not including either toxic auxiliary ligands in the framework and/or impregnated or coordinated harmful solvents in the pores. The measured surface area value for CaSyr-1 is just comparable with that reported for the γ-cyclodextrin macrocyclic CD-MOF-1. Regardless, CaSyr-1 exhibits a notably larger pore aperture diameter (1.4 nm) in comparison with CD-MOF-1 (0.42 and 0.78 nm), which would extend for the former, the scope of possible bioactive ingredients to be encapsulated.[6a,c,22]

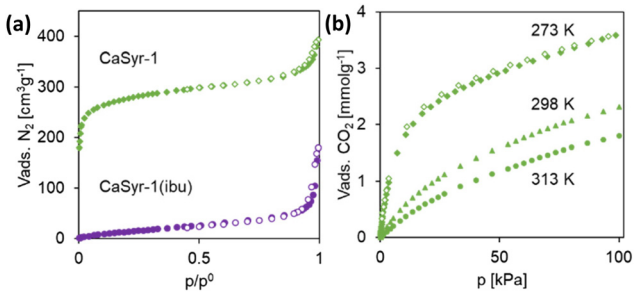

Fig. 4 Adsorption behavior: (a) N_2 isotherms at 77 K for pristine CaSyr-1 and impregnated CaSyr-1(ibu), and (b) CO_2 isotherm at 273, 298 and 313 K of CaSyr-1.

The lighter weight of Ca^{2+} with respect to transition metals offers gravimetric advantages for gas loading, which together with the large affinity of Ca^{2+} for CO_2, makes Ca-based MOFs suitable materials for CO_2 sorption. Uptakes in the order of 1–2 mmol g^{-1} (100 kPa and 273–298 K) are reported,[13] which could only be increased by synthetizing mixed-metal MOFs.[23] Remarkably, the monometallic CaSyr-1 bioMOF described in this work, with a CO_2 sorption of 3.7, 2.4 and 1.8 mmol g^{-1} at 100 kPa and 273, 298 and 313 K (Fig. 4b), respectively, outperform the values previously described for Ca-based MOFs (Table S2†). Actually, the found value of CO_2 sorption for CaSyr-1 is closer to that of basic adenine bioMOFs, specifically designed for this application,[24] and the industrially used activated carbon or zeolite 13X (*ca.* 4 mmol g^{-1}).[25] From the data extracted at different adsorption temperatures, the CO_2 enthalpy of adsorption (Q_{st}) could be estimated, giving rise to a value of *ca.* 18 J $mmol^{-1}$ (Fig. S7†) in the range of physisorption. The PXRD spectra of CaSyr-1 after these analyses indicate that CO_2 was desorbed without any structural modification of the adsorbent. For environmental and process cost reasons, in the application of CO_2 capture, the use of inexpensive renewable biolinkers for MOF design, such as that in CaSyr-1, is preferred *vs.* those derived from non-renewable petrochemical feedstocks.[2]

For adsorption-related applications, thermal stability plays an important role in ensuring the integrity of MOFs during interaction with an adsorbate and in the regeneration process of the material for further reuse.[26] Here, the thermal stability of CaSyr-1 was evaluated through thermogravimetric analysis (TGA) under N_2 flow (Fig. S8†). The weight decay at *ca.* 330 and 420 K is ascribed to the loss of EtOH and water molecules, respectively, both trapped in the cavities of the bioMOF during synthesis and manipulation, resulting in a total weight loss of about 20 wt%. The weight decrease does not involve any structural change in the framework of CaSyr-1, which was confirmed by a variable-temperature PXRD (VTPXRD) analysis, measured continuously from 298 to 500 K. Actually, no significant differences among the patterns recorded at the different temperatures were noticed (Fig. S9†). Hence, the removal of the solvent from the voids does not compromise the stability of the porous framework. The TGA suggests that CaSyr-1 is thermally stable up to *ca.* 600 K, the temperature at which the pyrolysis of the bioligand induces the degradation of the network. This notable thermal stability is usual in Ca-based

Open Access Article. Published on 02 bezna 2023. Downloaded on 20.10.2024 2:06:59.
This article is licensed under a Creative Commons Attribution-NonCommercial 3.0 Unported Licence.

Table 1 Representative porous biocompatible bioMOFs constructed from bioligands and their reported textural properties

BioMOF	Bioligand	Apparent BET surface area ($m^2\ g^{-1}$)	Micropore volume ($cm^3\ g^{-1}$)	Pore aperture diameter (nm)	Ref.
CaSyr-1	Syringate	1080	0.32	1.4	This work
CD-MOF-1	γ-Cyclodextrin	1220	0.47	0.42/0.78	6*a*
sc-CCMOF-1	Curcumine	350	0.10	N/A	6*c*
$[Cu_2(\mu_3\text{-ade})_2(\mu_2\text{-OOCCH}_3)_2]\cdot H_2O$	Adenine/acetate	505	0.17	N/A	22*a*
$\{[Zn(FDC)]\cdot H_2O\}_n$	2,5-Furandicarboxylate	780	N/A	0.63	22*b*
MOF-1201	L-Lactate	430	0.18	0.78	22*c*

MOFs containing O-donor linkers due to the ionic character of the formed Ca–O bonds.[13]

2.4. Biocompatibility and drug release

The focus on applications for the newly designed CaSyr-1 bioMOF is primarily directed to biomedicine. Although CaSyr-1 constituents are known to be non-toxic, it is of major importance to examine the bioMOF biocompatibility, since parameters such as constituents' interactions, particle size or trapped solvent residue could influence the overall cytotoxicity, evaluated in this work through the half maximal inhibitory concentration (IC_{50}). The IC_{50} for the bioMOF was calculated to be 9.6 mg cm^{-3}, close to the 7.8 mg cm^{-3} found for pristine H_2Syr (Fig. S10 and S11†) and far from the values considered cytotoxic,[27] which situates CaSyr-1 as a biocompatible platform ready for biomedical use.

The pristine bioMOF could be used to physiologically release Ca^{2+}, essential for a healthy skeleton, and Syr^{2-}, with a strong inhibition activity for COX-2 – recognized as the main anti-inflammatory target.[28] To advance the therapeutic properties of CaSyr-1, this bioMOF can be loaded with a wide range of drugs, taking advantage of its high porosity and large pore diameter, to develop a triply bioactive CaSyr-1(drug) system, *i.e.*, activity found in Ca^{2+}, Syr^{2-} and the impregnated drug (Fig. 5).

Therapeutic regimens based on the use of multicomponent drugs are an effective alternative to the one-target single molecular entities, since multiple targets can be involved in the treatment of a particular disease.[29] Herein, this possibility was experimentally tested, demonstrating the easy impregnation of ibuprofen in CaSyr-1 using non-toxic supercritical CO_2 ($scCO_2$). In the impregnated sample, designated as CaSyr-1 (ibu), ibuprofen was assumed to reside solely in the pores of the bioMOF, since no sign of drug recrystallization outside the nanoparticles was noticed in the SEM images (Fig. S12†) or in the PXRD pattern (Fig. S13†). For CaSyr-1(ibu), the adsorption branch of the N_2 isotherm displayed a complete drop in gas adsorption at low relative pressures (Fig. 4a), which indicates that the micropores were already filled with the drug. The percentage of ibuprofen in CaSyr-1(ibu) was estimated by ^1H nuclear magnetic resonance (^1H-NMR) after sample treatment with hydrofluoric acid. The ^1H-NMR spectrum shows a 3 : 1 molar ratio of syringate : ibuprofen, which equates to a *ca.* 21 wt% ibuprofen loading (Fig. S14–S16†), similar to other reported values.[30] By modifying the experimental conditions in the $scCO_2$ approach, the ibuprofen loading can be controlled in the range *ca.* 10–25 wt%.

The multicomponent release of CaSyr-1(ibu) was studied here by suspending the impregnated bioMOF in a solution of PBS (buffer pH = 7.4) in D_2O at 310 K for 1 day. During this period, several aliquots were collected at different times and measured by NMR (Fig. S17–S20†). Interestingly, in all the cases (from 10 min to 1 day), the signals assigned to both ibuprofen and H_2Syr were visible, and the corresponding integration peaks ratio remained nearly constant (*ca.* 2.5–2.8 : 1, syringate : ibuprofen), with values consistent with the initial molar ratio in the solid form (3 : 1). This indicates not only a fast delivery of the cargo, but also of CaSyr-1 building blocks, induced by the degradation of the framework under physiological conditions. For small hydrophobic drugs, such as ibuprofen, physiologically unstable MOFs have already been contemplated as potential delivery vehicles to increase their bioavailability.[31] This favourable burst phenomenon is promoted by the release of the drug confined in the bioMOF in the molecular form, making it dissolve much more easily than crystalline drugs.

The IC_{50} of the impregnated sample was found to be 5 mg cm^{-3}, almost half of the CaSyr-1 IC_{50} (Fig. S10†). The overall cytotoxicity increases due to the inherent mild toxicity of ibuprofen, with a calculated IC_{50} of 1.9 mg cm^{-3} (Fig. S11†). Ibuprofen, even as one of the most prescribed nonsteroidal anti-inflammatory drugs, must be administered with caution due to its negative secondary effects related to dosage.[32] In the designed CaSyr-1(ibu), the merging of the COX-2 anti-inflammatory activity of syringic acid and that of ibuprofen is

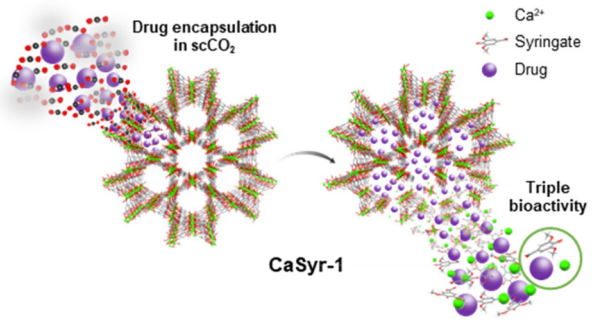

Fig. 5 Schematic representation of drug encapsulation in CaSyr-1 and subsequent triply bioactive release.

Open Access Article. Published on 02 bezna 2023. Downloaded on 20.10.2024 2:06:59.
This article is licensed under a Creative Commons Attribution-NonCommercial 3.0 Unported Licence.

expected to result in a positive decrease in the required dosage of ibuprofen. Moreover, the use of ibuprofen is associated with increased blood pressure and must be excluded from patients diagnosed with hypertension, *ca.* 30% of the worldwide adult population.[33] Quite the reverse, CaSyr-1 could help in decreasing blood pressure, since both calcium and syringic acid have demonstrated anti-hypertensive effects.[34] Hence, the population targeted with the administration of ibuprofen could be increased by embedding hypertensive ibuprofen into the CaSyr-1 anti-hypertensive bioMOF.

3. Conclusions

Homogeneously sized nanoparticles of CaSyr-1 can be easily prepared from renewable biocompatible components in a sustainable strategy with a large space–time yield. These processing aspects, along with the displayed exceptionally high surface areas and pore sizes, make this material a promising candidate for adsorption. Two main application areas have been envisaged: the reversible adsorption of CO_2 and the encapsulation of bioactive ingredients in the structure. It must be emphasized that CaSyr-1 enables the development of triply bioactive entities with promising activity as a multicomponent drug system.

4. Experimental section

4.1. Materials

The employed reactants for the CaSyr-1 preparation were syringic acid (H_2Syr 98%, abcr) and either calcium acetylacetonate ($Ca(acac)_2$ 98%, abcr) or calcium chloride ($CaCl_2$ > 95%, Merck). The used solvents were absolute ethanol (EtOH, Scharlab) and dimethylformamide (DMF, abcr). For drug impregnation, the active compound was (*S*)-(+)-ibuprofen (ibu 99%, Sigma-Aldrich) dissolved in supercritical CO_2 ($scCO_2$), which was provided as compressed CO_2, 99.95 wt%, by Carburos Metálicos S.A.

4.2. Synthetic procedure

CaSyr-1 nanopowder synthesis. The synthesis of CaSyr-1 nanopowder was carried out in EtOH, starting from equimolar ratios of the reagents, optimizing the volume of the solvent as the main parameter as follows.

1 mL of EtOH. 1.0 mmol of $Ca(acac)_2$ and 1.0 mmol of H_2Syr were introduced into a vial containing 1 mL of EtOH. The attained molar ratio of reactants : EtOH was 1 : 8. The slurry was sonicated for 1 min and left to rest for 10 min at room temperature. The obtained crude product was washed three times with 10 mL of EtOH by vortex-centrifugation and dried under vacuum (yield = 82 wt%).

10 mL of EtOH (the optimized protocol). 1.0 mmol of $Ca(acac)_2$ and 1.0 mmol of H_2Syr were separately introduced into two vials containing 5 mL of EtOH each and sonicated for 1 min, resulting in a suspension and a solution, respectively. The contents of both vials were then mixed, attaining a molar ratio of reactants : EtOH of 1 : 80, and left to rest for 10 min at room temperature. The obtained crude product was washed three times with 10 mL of EtOH by vortex-centrifugation and finally dried under vacuum (yield = 87 wt%).

CaSyr-1 large crystal synthesis. For the synthesis of CaSyr-1 large crystals, suitable for structure elucidation through synchrotron radiation, 0.5 mmol of $CaCl_2$ and 0.5 mmol of H_2Syr were initially dissolved in 15 and 10 mL of DMF, respectively. Each vial was sonicated for 5 min. Both solutions were then mixed in a 50 mL Pyrex glass vial, tightly closed, and introduced into an oven at 393 K for 7 days. After this period, the recovered product was washed twice with 25 mL of DMF, filtered and dried under vacuum. The crystals were preserved in Fomblin® Y oil for further structural elucidation.

CaSyr-1 impregnation, CaSyr-1(ibu). Prior to the impregnation process, CaSyr-1 nanopowder was activated under vacuum up to 15 Pa in an oven at 373 K for 6 h, in order to remove the solvent from the pores. The impregnation of CaSyr-1 with ibu was run in $scCO_2$. In a typical experiment, a 100 mL high-pressure vessel was loaded with a short beaker containing 185 mg of ibu (0.90 mmol) and a stir bar. A table grid, supporting a rolled filter paper enclosing 150 mg (0.60 mmol, considering the empirical formulae) of activated CaSyr-1, was placed on the beaker inside the reactor. Once closed, liquid CO_2 was flushed into the vessel at 6.0 MPa and heated at 313 K. The pressure was increased to 15 MPa by compressing CO_2 with a Teledyne Isco 260D syringe pump and the stirring was adjusted to 500 rpm. These working conditions were maintained for a period of 20 h. After this time, the reactor was isothermally depressurized and then cooled down to room temperature. Finally, the impregnated product was recovered.

4.3. Characterization techniques

Single crystal X-ray diffraction. Single-crystal X-ray diffraction (SCXRD) experiments for the structural elucidation of the CaSyr-1 compound were performed in the XALOC beamline at the ALBA synchrotron.[35] Data were collected at 100 K with a 0.72931 Å wavelength using a Dectris Pilatus 6M detector placed at 120 mm from the sample. ϕ scans were performed from 0 to 360° in steps of 0.5° with a collection time of 0.15° per step. The scan was repeated at three different κ angles (0, 45 and 90°) and merged afterwards to increase the completeness and redundancy when possible. Data were indexed, integrated and scaled using the XDS software.[36] The crystal structure was solved by intrinsic phasing and refined with SHELXL (version 2014/7)[37] using Olex2 as the graphical interface.[38]

Powder X-ray diffraction. Powder X-ray diffraction patterns (PXRD) were recorded at room temperature in a Siemens D5000 diffractometer with Cu Kα incident radiation. The selected 2θ range for data acquisition was 5–30° in steps of 0.02° s^{-1}. For the sample prepared in DMF involving large crystals, the product was ground by hand in an agate pestle prior to PXRD characterization.

Variable-temperature PXRD. The variable-temperature PXRD (VTPXRD) measurements were performed at the BL16-NOTOS

Open Access Article. Published on 02 bezna 2023. Downloaded on 20.10.2024 2:06:59.
This article is licensed under a Creative Commons Attribution-NonCommercial 3.0 Unported Licence.

beamline of the ALBA synchrotron, from 298 up to 500 K. Data were collected at 20 keV (0.62074 Å wavelength) in the transmission mode using a Mythen-II detector (6 modules at 535 mm from the sample). The powdered sample was placed inside an *ad hoc* capillary reaction cell (fused silica capillary with 0.7 and 0.85 nm inner and outer diameters, respectively) with a capillary connected online to both a gas-handling and a vacuum line. An Oxford Cryostream 700 instrument was used to control the temperature of the sample.

Microscopy. CaSyr-1 large crystals were optically analyzed with an Olympus IX53 inverted microscope connected to a XC30 camera. The crystal morphology of the nanopowder was observed by scanning electron microscopy (SEM) in a Quanta FEI 200 FEG-ESEM microscope. For better resolution, the sample was coated with Au/Pd. The histograms of the particle-size distribution were obtained by measuring >200 discrete particlesin images taken with a transmission electron microscope (TEM; JEOL 1210) using the ImageJ program.

Dynamic light scattering. The particle-size distribution in suspension was estimated by the dynamic light scattering (DLS) method, using a Zetasizer Nano ZS Malvern Inst. Prior to the measurement, CaSyr-1 was suspended in EtOH and sonicated for 1 h.

Gas adsorption. The porosity of the samples was determined by analysing the N_2 adsorption–desorption isotherms recorded at 77 K using ASAP 2020 Micromeritics Inc. equipment. The apparent specific surface area was calculated by applying the BET (Brunauer–Emmett–Teller) equation or the Langmuir model. The micropore volume was determined by the *t*-plot method. The CO_2 sorption capacity was assessed by analysing the isotherms at 273, 298 and 313 K up to 0.1 MPa. In both cases, the samples were first degassed at 373 K under high vacuum (10 Pa) for 20 h. The CO_2 enthalpy of adsorption (Q_{st}) was determined through the graphical representation of the pressure logarithm ($\ln p$) for a given adsorbed amount (n) as a function of the reciprocal temperature ($1/T$). The Q_{st} at a specific adsorbate loading was then estimated using the Clausius–Clapeyron equation (eqn (1)):

$$Q_{st}(n) = -R \ln(p_2/p_1)(T_1T_2/(T_2 - T_1)) \quad (1)$$

Elemental analysis. The chemical composition of CaSyr-1 nanopowder, regarding carbon and hydrogen, was estimated by elemental analysis (EA). Data were recorded in a Flash *Smart*™ elemental analyzer. The results were compared with the theoretical values calculated from the crystallographic formulae contained in the generated CIF from single crystal structural data (without considering the solvent in the pores).

Thermogravimetric analysis. The thermal stability of CaSyr-1 was evaluated by thermogravimetric analysis (TGA) under N_2 flow using a SDT 650-TA instrument.

^{1}H-nuclear magnetic resonance. Proton nuclear magnetic resonance (^{1}H-NMR) was employed to quantify the content of ibuprofen in the impregnated sample CaSyr-1(ibu). In order to release all the ibu and H_2Syr from CaSyr-1(ibu), 20 mg of the sample was suspended in methanol, and 4 drops of HF (40 v% in water) were added. The mixture was heated at 333 K overnight to evaporate the solvent and excess HF, resulting in a crude product that contained CaF_2, protonated H_2Syr and ibuprofen. DMSO-d_6 was added to dissolve the organic components, and the subsequent suspension was filtered before transferring it to the ^{1}H-NMR tube in order to remove the precipitated calcium salt. The analysis was carried out in a Bruker Avance NEO 300 MHz. Both, ibuprofen and syringic acid exhibited well-defined 6H signals in the ^{1}H-NMR spectrum, corresponding to two methyls and two methoxides at δ = 0.86 and 3.80 ppm, respectively (Fig. S14 and S15†). Hence, in CaSyr-1(ibu), the molar ratio of ibu with respect to H_2Syr can be estimated by comparing the integration of the signal at 0.86 ppm with the integration of the signal at 3.80 ppm (Fig. S16†).

4.4. Bioactive release and biocompatibility assays

Bioactive release. The release of the organic bioactive components present in CaSyr-1(ibu) was tracked by ^{1}H-NMR, utilizing the same spectrometer as in the previous section. For that, 25 mg of CaSyr-1(ibu), corresponding to the IC_{50}, was suspended in 5 mL of PBS in D_2O (buffer pH = 7.4) under stirring at 200 rpm for 1 day at 310 K. The system was maintained under inert conditions to avoid the exchange of D_2O with H_2O from the air. During this period, four aliquots were collected at different times, *i.e.*, 10 min, 1, 3 and 24 h, and centrifuged to remove the precipitate and characterized by ^{1}H-NMR. The molar ratio of the syringate with respect to ibuprofen was estimated as in the previous section.

Cell culture. Biocompatibility was tested on a human osteosarcoma cell line (MG63, ATCC CRL1427). MG63 cells were cultured on the MEM NEAA medium (Sigma Aldrich), supplemented with 10 wt% of fetal bovine serum (FBS, Sigma), 1 wt% penicillin/streptomycin (Invitrogen) and 2 wt% L-glutamine (Invitrogen). Cells were cultured at 310 K and 5 v% CO_2 in a humidified chamber until confluence before the assays. Cells were used from 4 to 8 passages in all the experiments.

Toxicity tests. For pristine syringic acid and ibuprofen compounds, MG63 cells were cultured on a 96 well-plate at 100 000 cells per cm^3 and incubated at 310 K and 5 v% CO_2. After 24 h, the medium was replaced by seriated dilutions of syringic acid in culture medium and ibuprofen in 1 v% DMSO added to the culture medium. The cells were incubated at 310 K and 5 v% CO_2 for 24 h. MG63 cells in culture medium and 1 v% DMSO in culture medium were used as the control systems. After 24 h, the medium was replaced by the culture medium without phenol red (Sigma Aldrich).

For CaSyr-1 and CaSyr-1(ibu), 200 μL of MG63 cells was cultured on transwell insets (collagen coated, cut-off = 0.4 μm, diameter = 6.5 mm, Costar) at 100 000 cells per cm^3. The insets were incubated in a 48-well plate with 400 μL of culture medium and at 310 K and 5 v% CO_2. After 24 h, the medium of the inset was replaced by fresh medium, and the medium of the well plate was replaced by seriated dilutions of CaSyr-1 and CaSyr-1(ibu) in culture medium (starting at 25 mg cm^{-3}). After

Open Access Article. Published on 02 bezna 2023. Downloaded on 20.10.2024 2:06:59.
This article is licensed under a Creative Commons Attribution-NonCommercial 3.0 Unported Licence.

24 h, all the media were replaced by culture medium without phenol red.

Cell viability. In the different studied systems, cell viability was analysed by adding Alamar Blue (1) ISO 10993-5:2009 (AB, Invitrogen)[39] at 10 v% and culturing the cells at 310 K for 4 h. After this time, the cell viability was measured using a plate reader (Biotek Synergy HT spectrophotometer) with laser excitation at 590 nm and measuring the emitted fluorescence at 530 nm. The cell viability (%) was calculated using the following equation (eqn (2)):

$$\text{Cell viability } (\%) = 100 \times (\text{ODS} - \text{ODB})/(\text{ODC} - \text{ODB}) \quad (2)$$

where ODS, ODB, and ODC represent the emitted fluorescence at 530 nm for the sample (S), blank (B, culture medium without cells), and control (C), respectively. The experiments were conducted in triplicate for each sample, and the data obtained were expressed as mean values ± SD.

Conflicts of interest

There are no conflicts to declare.

Acknowledgements

This work was supported by the Spanish Ministry of Science and Innovation MICINN through the Severo Ochoa Program for Centers of Excellence (CEX2019–000917-S), by the Spanish National Plan of Research with projects PID2020-115631GB-I00 and PID2020-114086RB-100 and by CIBER (Spain) – Consorcio Centro de Investigación Biomédica en Red (Ref. CB06/01/0013), Instituto de Salud Carlos III, MICINN. This research work was performed in the framework of the Nanomedicine CSIC HUB (Ref. 202180E048). ALBA synchrotron is acknowledged for the provision of beam time. A. R. acknowledges the financial support of FPI 2019 grant. This work has been performed in the framework of the doctoral program "Chemistry" of the Universitat Autònoma de Barcelona by A. R.

This work is dedicated to the memory of Blanca Vázquez-Lasa, who was a long-term collaborator of many of the authors. We feel grateful for having had the chance to interact with Blanca, a woman of great insight and sweetness. Though she did not witness the publication of this article, she motivated much of the work presented here, and accompanied it for as long as her health permitted. Both as scientists and as personal acquaintances, we miss Blanca greatly, and we would like to express our condolences to her family and friends.

References

1 (*a*) S. T. Meek, J. A. Greathouse and M. D. Allendorf, Metal–organic frameworks: A Rapidly growing class of versatile nanoporous materials, *Adv. Mater.*, 2011, **23**, 249–267; (*b*) H. C. Zhou, J. R. Long and O. M. Yaghi, Introduction to metal–organic frameworks, *Chem. Rev.*, 2012, **112**, 673–674; (*c*) P. Horcajada, R. Gref, T. Baati, P. K. Allan, G. Maurin, P. Couvreur, G. Férey, R. E. Morris and C. Serre, Metal–organic frameworks in biomedicine, *Chem. Rev.*, 2012, **112**, 1232–1268.

2 A. Zulys, F. Yulia, N. Muhadzib and Nasruddin, Biological metal–organic frameworks (Bio-MOFs) for CO_2 capture, *Ind. Eng. Chem. Res.*, 2021, **60**, 37–51.

3 A. C. McKinlay, R. E. Morris, P. Horcajada, G. Férey, R. Gref, P. Couvreur and C. Serre, BioMOFs: metal–organic frameworks for biological and medical applications, *Angew. Chem., Int. Ed.*, 2010, **49**, 6260–6266.

4 (*a*) I. Abánades Lázaro and R. S. Forgan, Application of zirconium MOFs in drug delivery and biomedicine, *Coord. Chem. Rev.*, 2019, **380**, 230–259; (*b*) W. Cai, J. Wang, C. Chu, W. Chen, C. Wu and G. Liu, Metal–organic framework-based stimuli-responsive systems for drug delivery, *Adv. Sci.*, 2019, **6**, 1801526; (*c*) A. Bieniek, A. P. Terzyk, M. Wiśniewski, K. Roszek, P. Kowalczyk, L. Sarkisov, S. Keskin and K. Kaneko, MOF materials as therapeutic agents, drug carriers, imaging agents and biosensors in cancer biomedicine: Recent advances and perspectives, *Prog. Mater. Sci.*, 2021, **117**, 100743.

5 S. Rojas, T. Devic and P. Horcajada, Metal organic frameworks based on bioactive components, *J. Mater. Chem. B*, 2017, **5**, 2560–2573.

6 (*a*) R. A. Smaldone, R. S. Forgan, H. Furukawa, J. J. Gassensmith, A. M. Z. Slawin, O. M. Yaghi and J. F. Stoddart, Metal–organic frameworks from edible natural products, *Angew. Chem., Int. Ed.*, 2010, **49**, 8630–8634; (*b*) H. Su, F. Sun, J. Jia, H. He, A. Wang and G. Zhu, A highly porous medical metal–organic framework constructed from bioactive curcumin, *Chem. Commun.*, 2015, **51**, 5774–5777; (*c*) N. Portolés-Gil, A. Lanza, N. Aliaga-Alcalde, J. A. Ayllón, M. Gemmi, E. Mugnaioli, A. M. López-Periago and C. Domingo, Crystalline curcumin BioMOF obtained by precipitation in supercritical CO_2 and structural determination by electron diffraction tomography, *ACS Sustainable Chem. Eng.*, 2018, **6**, 12309–12319; (*d*) S. Quaresma, V. André, A. M. M. Antunes, S. M. F. Vilela, G. Amariei, A. Arenas-Vivo, R. Rosal, P. Horcajada and M. T. Duarte, Novel antibacterial azelaic acid BioMOFs, *Cryst. Growth Des.*, 2020, **20**, 370–382.

7 (*a*) J. An, S. J. Geib and N. L. Rosi, Cation-triggered drug release from a porous zinc-adeninate metal–organic framework, *J. Am. Chem. Soc.*, 2009, **131**, 8376–8377; (*b*) J. An, O. K. Farha, J. T. Hupp, E. Pohl, J. I. Yeh and N. L. Rosi, Metal-adeninate vertices for the construction of an exceptionally porous metal–organic framework, *Nat. Commun.*, 2012, **3**, 604.

8 (*a*) M. Giménez-Marqués, T. Hidalgo, C. Serre and P. Horcajada, Nanostructured metal–organic frameworks and their bio-related applications, *Coord. Chem. Rev.*, 2016, **307**, 342–360; (*b*) C. Tamames-Tabar, D. Cunha, E. Imbuluzqueta, F. Ragon, C. Serre, M. J. Blanco-Prieto and P. Horcajada, Cytotoxicity of nanoscaled metal–organic frameworks, *J. Mater. Chem. B*, 2014, **2**, 262–271.

Open Access Article. Published on 02 bezna 2023. Downloaded on 20.10.2024 2:06:59.
This article is licensed under a Creative Commons Attribution-NonCommercial 3.0 Unported Licence.

9 (*a*) P. Li, R. C. Klet, S. Y. Moon, T. C. Wang, P. Deria, A. W. Peters, B. M. Klahr, H. J. Park, S. S. Al-Juaid, J. T. Hupp and O. K. Farha, Synthesis of nanocrystals of Zr-based metal–organic frameworks with Csq-Net: Significant enhancement in the degradation of a nerve agent simulant, *Chem. Commun.*, 2015, **51**, 10925–10928; (*b*) C. R. Marshall, S. A. Staudhammer and C. K. Brozek, Size control over metal–organic framework porous nanocrystals, *Chem. Sci.*, 2019, **10**, 9396–9408; (*c*) M. Chang, T. Wei, D. Liu, J. X. Wang and J. F. Chen, A general strategy for instantaneous and continuous synthesis of ultrasmall metal–organic framework nanoparticles, *Angew. Chem., Int. Ed.*, 2021, **60**, 26390–26396.

10 K. Pobłocki, J. Drzeżdżon, B. Gawdzik and D. Jacewicz, Latest trends in the large-scale production of MOFs in accordance with the principles of green chemistry, *Green Chem.*, 2022, **24**, 9402–9427.

11 X. Zhang, Z. Chen, X. Liu, S. L. Hanna, X. Wang, R. Taheri-Ledari, A. Maleki, P. Li and O. K. Farha, A historical overview of the activation and porosity of metal–organic frameworks, *Chem. Soc. Rev.*, 2020, **49**, 7406–7427.

12 A. Carné-Sánchez, I. Imaz, M. Cano-Sarabia and D. Maspoch, Spray-drying strategy for synthesis of nanoscale metal–organic frameworks and their assembly into hollow superstructures, *Nat. Chem.*, 2013, **5**, 203–211.

13 S. Xian, Y. Lin, H. Wang and J. Li, Calcium-based metal–organic frameworks and their potential applications, *Small*, 2021, **17**, 2005165.

14 G. Cormick and J. M. Belizán, Calcium intake and health, *Nutrients*, 2019, **11**, 1606.

15 (*a*) C. Srinivasulu, M. Ramgopal, G. Ramanjaneyulu, C. M. Anuradha and C. Suresh Kumar, Syringic acid (SA) – A review of its occurrence, biosynthesis, pharmacological and industrial importance, *Biomed. Pharmacother.*, 2018, **108**, 547–557; (*b*) A. C. Mirza and S. S. Panchal, Safety evaluation of syringic acid: Subacute oral toxicity studies in Wistar rats, *Heliyon*, 2019, **5**, e02129.

16 (*a*) Z. Heren, H. Paşaoğlu, G. Kaştaş, L. Vurucu and O. Büyükgüngör, Synthesis, spectral and thermal properties, and crystal structure of bis(ethylenediamine) (aqua)copper(II) (bis)syringate ethylenediamine dihydrate $[Cu(en)_2(H_2O)](Sy)_2(en)(H_2O)_2$, *Z. Naturforsch., B: Chem. Sci.*, 2006, **61**, 287–291; (*b*) Z. Q. Huang, B. Wang, D. S. Pan, L. L. Zhou, Z. H. Guo and J. L. Song, Rational design of a N,S co-doped supermicroporous CoFe–organic framework platform for water oxidation, *ChemSusChem*, 2020, **13**, 2564–2570.

17 K. Tekin, N. Hao, S. Karagoz and A. J. Ragauskas, Ethanol: A promising green solvent for the deconstruction of lignocellulose, *ChemSusChem*, 2018, **11**, 3559–3575.

18 W. Bao, F. Tian, C. Lyu, B. Liu, B. Li, L. Zhang, X. Liu, F. Li, D. Li, X. Gao, S. Wang, W. Wei, X. Shi and Y. Li, Experimental and theoretical explorations of nanocarriers' multistep delivery performance for rational design and anticancer prediction, *Sci. Adv.*, 2021, **7**, eaba2458.

19 (*a*) S. Mukherjee, J. Lu, G. Velmurugan, S. Singh, G. Rajaraman, J. Tang and S. K. Ghosh, Influence of tuned linker functionality on modulation of magnetic properties and relaxation dynamics in a family of six isotypic Ln_2 (Ln = Dy and Gd) complexes, *Inorg. Chem.*, 2016, **55**, 11283–11298; (*b*) T. J. Feuerstein, R. Müller, C. Barner-Kowollik and P. W. Roesky, Investigating the photochemistry of spiropyran metal complexes with online LEDNMR, *Inorg. Chem.*, 2019, **58**, 15479–15486.

20 (*a*) N. J. Ghimire and I. I. Mazin, Topology and correlations on the kagome lattice, *Nat. Mater.*, 2020, **19**, 137–138; (*b*) J. E. Mondloch, W. Bury, D. Fairen-Jimenez, S. Kwon, E. J. Demarco, M. H. Weston, A. A. Sarjeant, S. T. Nguyen, P. C. Stair, R. Q. Snurr, O. K. Farha and J. T. Hupp, Vapor-phase metalation by atomic layer deposition in a metal–organic framework, *J. Am. Chem. Soc.*, 2013, **135**, 10294–10297.

21 (*a*) T. Li, M. T. Kozlowski, E. A. Doud, M. N. Blakely and N. L. Rosi, Stepwise ligand exchange for the preparation of a family of mesoporous MOFs, *J. Am. Chem. Soc.*, 2013, **135**, 11688–11691; (*b*) K. Wang, D. Feng, T. F. Liu, J. Su, S. Yuan, Y. P. Chen, M. Bosch, X. Zou and H. C. Zhou, A series of highly stable mesoporous metalloporphyrin Fe-MOFs, *J. Am. Chem. Soc.*, 2014, **136**, 13983–13986.

22 (*a*) S. Pérez-Yañez, G. Beobide, O. Castillo, J. Cepeda, A. Luque, A. T. Aguayo and P. Román, Open-framework copper adeninate compounds with three-dimensional microchannels tailored by aliphatic monocarboxylic acids, *Inorg. Chem.*, 2011, **50**, 5330–5332; (*b*) D. Y. Ma, J. Xie, Z. Zhu, H. Huang, Y. Chen, R. Su and H. Zhu, Drug delivery and selective CO_2 adsorption of a bio-based porous zinc-organic framework from 2,5-furandicarboxylate ligand, *Inorg. Chem. Commun.*, 2017, **86**, 128–132; (*c*) J. Yang, C. A. Trickett, S. B. Alahmadi, A. S. Alshammari and O. M. Yaghi, Calcium L-lactate frameworks as naturally degradable carriers for pesticides, *J. Am. Chem. Soc.*, 2017, **139**, 8118–8121.

23 D. Saha, T. Maity and S. Koner, Metal–organic frameworks based on alkaline earth metals – Hydrothermal synthesis, X-ray structures, gas adsorption, and heterogeneously catalyzed hydrogenation reactions, *Eur. J. Inorg. Chem.*, 2015, **2015**, 1053–1064.

24 J. An, R. P. Fiorella, S. J. Geib and N. L. Rosi, Synthesis, structure, assembly, and modulation of the CO_2 adsorption properties of a zinc–adeninate macrocycle, *J. Am. Chem. Soc.*, 2009, **131**, 8401–8403.

25 L. Hauchhum and P. Mahanta, Carbon dioxide adsorption on zeolites and activated carbon by pressure swing adsorption in a fixed bed, *Int. J. Energy Environ. Eng.*, 2014, **5**(4), 349–356.

26 H. U. Escobar-Hernandez, L. M. Pérez, P. Hu, F. A. Soto, M. I. Papadaki, H. C. Zhou and Q. Wang, Thermal stability of metal–organic frameworks (MOFs): Concept, determination, and model prediction using computational chemistry and machine learning, *Ind. Eng. Chem. Res.*, 2022, **61**, 5853–5862.

27 D. Campoccia, S. Ravaioli, S. Santi, V. Mariani, C. Santarcangelo, A. De Filippis, L. Montanaro,

Open Access Article. Published on 02 bezna 2023. Downloaded on 20.10.2024 2:06:59.
This article is licensed under a Creative Commons Attribution-NonCommercial 3.0 Unported Licence.

C. R. Arciola and M. Daglia, Exploring the anticancer effects of standardized extracts of poplar-type propolis: In vitro cytotoxicity toward cancer and normal cell lines, *Biomed. Pharmacother.*, 2021, **141**, 111895.

28 (*a*) R. Stanikunaite, S. I. Khan, J. M. Trappe and S. A. Ross, Cyclooxygenase-2 inhibitory and antioxidant compounds from the truffle *Elaphomyces granulatus*, *Phytother. Res.*, 2009, **23**, 575–578; (*b*) M. H. Lee, H. Kang, K. Lee, G. Yang, I. Ham, Y. Bu, H. Kim and H. Y. Choi, The aerial part of *Taraxacum coreanum* extract has an anti-inflammatory effect on peritoneal macrophages in vitro and increases survival in a mouse model of septic shock, *J. Ethnopharmacol.*, 2013, **146**, 1–8.

29 C. T. Keith, A. A. Borisy and B. R. Stockwell, Multicomponent therapeutics for networked systems, *Nat. Rev. Drug Discovery*, 2005, **4**, 71–78.

30 (*a*) P. Horcajada, C. Serre, G. Maurin, N. A. Ramsahye, F. Balas, M. Vallet-Regí, M. Sebban, F. Taulelle and G. Férey, Flexible porous metal–organic frameworks for a controlled drug delivery, *J. Am. Chem. Soc.*, 2008, **130**, 6774–6780; (*b*) K. J. Hartlieb, D. P. Ferris, J. M. Holcroft, I. Kandela, C. L. Stern, M. S. Nassar, Y. Y. Botros and J. F. Stoddart, Encapsulation of ibuprofen in CD-MOF and related bioavailability studies, *Mol. Pharm.*, 2017, **14**, 1831–1839.

31 K. Suresh and A. J. Matzger, Enhanced drug delivery by dissolution of amorphous drug encapsulated in a water unstable metal–organic framework (MOF), *Angew. Chem., Int. Ed.*, 2019, **58**, 16790–16794.

32 S. Harirforoosh, W. Asghar and F. Jamali, Adverse effects of nonsteroidal antiinflammatory drugs: An update of gastrointestinal, cardiovascular and renal complications, *J. Pharm. Pharm. Sci.*, 2013, **16**, 821–847.

33 (*a*) K. T. Mills, A. Stefanescu and J. He, The global epidemiology of hypertension, *Physiol. Behav.*, 2016, **176**, 139–148; (*b*) F. Ruschitzka, J. S. Borer, H. Krum, A. J. Flammer, N. D. Yeomans, P. Libby, T. F. Lüscher, D. H. Solomon, M. E. Husni, D. Y. Graham, D. A. Davey, L. M. Wisniewski, V. Menon, R. Fayyad, B. Beckerman, D. Iorga, A. M. Lincoff and S. E. Nissen, Differential blood pressure effects of ibuprofen, naproxen, and celecoxib in patients with arthritis: The PRECISION-ABPM (Prospective Randomized Evaluation of Celecoxib Integrated Safety Versus Ibuprofen or Naproxen Ambulatory Blood Pressure Measurement), *Eur. Heart J.*, 2017, **38**, 3282–3292.

34 (*a*) H. Nakamura, H. Tsujiguchi, A. Hara, Y. Kambayashi, S. Miyagi, T. T. T. Nguyen, K. Suzuki, Y. Tao, Y. Sakamoto, Y. Shimizu, N. Yamamoto and H. Nakamura, Dietary calcium intake and hypertension: Importance of serum concentrations of 25-hydroxyvitamin D., *Nutrients*, 2019, **11**, 911; (*b*) S. Kumar, P. Prahalathan and B. Raja, Syringic acid ameliorates L-NAME-induced hypertension by reducing oxidative stress, *Naunyn-Schmiedebergs Arch. Pharmacol.*, 2012, **385**, 1175–1184.

35 J. Juanhuix, F. Gil-Ortiz, G. Cuní, C. Colldelram, J. Nicolás, J. Lidón, E. Boter, C. Ruget, S. Ferrer and J. Benach, Developments in optics and performance at BL13-XALOC, the macromolecular crystallography beamline at the ALBA synchrotron, *J. Synchrotron Radiat.*, 2014, **21**, 679–689.

36 W. Kabsch, XDS, *Acta Crystallogr., Sect. D: Biol. Crystallogr.*, 2010, **66**, 125–132.

37 G. M. Sheldrick, Crystal structure refinement with SHELXL, *Acta Crystallogr., Sect. A: Found. Crystallogr.*, 2015, **71**, 3–8.

38 O. V. Dolomanov, L. J. Bourhis, R. J. Gildea, J. A. K. Howard and H. Puschmann, OLEX2: A complete structure solution, refinement and analysis program, *J. Appl. Crystallogr.*, 2009, **42**, 339–341.

39 International Standard ISO 10993-5. Third Edition 2009-06-01.